analytical chemistry

pubs.acs.org/ac Article

Dual-Mechanism-Driven Strategy for High-Coverage Detection of Serum Lipids on a Novel SALDI-MS Target

Xuetong Qu, Tao Wang, Xingyue Liu, Xinrong Jiang, Xiao Liang,* and Jianmin Wu*

Cite This: https://doi.org/10.1021/acs.analchem.1c04929 Read Online

ACCESS | Metrics & More | Article Recommendations | Supporting Information

ABSTRACT: Serum lipid metabolites have been emerging as ideal biomarkers for disease diagnosis and prediction. In the current stage, nontargeted or targeted lipidomic research mainly relies on a liquid chromatography−mass spectrometry (LC−MS) platform, but future clinical applications need more robust and high-speed platforms. Surface-assisted laser desorption ionization mass spectrometry (SALDI-MS) has shown excellent advantages in the high-speed analysis of lipid metabolites. However, the platform in the positive ion mode is more inclined to target a certain class of lipids, leading to the low coverage of lipid detection and limiting its practical translation to clinical applications. Herein, we proposed a dual-mechanism-driven strategy for high-coverage detection of serum lipids on a novel SALDI-MS target, which is a composite nanostructure comprising vertical silicon nanowires (VSiNWs) decorated with AuNPs and polydopamine (VSiNW-Au-PDA). The performance of laser desorption and ionization on the target can be enhanced by charge-driven desorption coupled with thermal-driven desorption. Simultaneous detection of 236 serum lipids (S/N ≥ 5) including neutral and polar lipids can be achieved in the positive ion mode. Among these, 107 lipid peaks were successfully identified. When combined with VSiNW-Au-PDA and VSiNW chips, 479 lipid peaks can be detected in serum samples in positive and negative ion modes, respectively. Based on the platform, serum samples from 57 hepatocellular carcinoma (HCC) patients and 76 healthy controls were analyzed. After data mining, 14 lipids containing different lipid types (TAG, CE, PC) were selected as potential lipidomic biomarkers. With the assistance of an artificial neural network, a diagnostic model with a sensitivity of 92.7% and a specificity of 96% was constructed for HCC diagnosis.

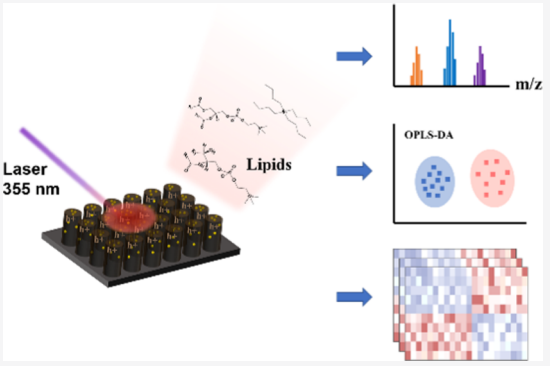

Clinical lipidomics has attracted wide attention because the composition and structure variance of lipid molecules are highly related to physiological and pathological changes in the human body. Emerging lipid biomarkers related to different types or stages of tumors have been explored in recent years.[1,2] Lipid molecules can be divided into two categories including polar lipids and neutral lipids, which can be further divided into eight categories according to their chemical structure, hydrophilicity, and hydrophobicity.[3] Polar lipids mainly include glycerophospholipids and sphingolipids, whereas neutral lipids mainly include glycerolipids and sterol lipids. These four major classes of lipids have been frequently investigated as potential tumor-related biomarkers in lipidomic research.[4,5] For example, the changes of LPE (18:1), PE (P-40:3), CE (18:2), and SM (22:0) in serum can distinguish lung cancer patients from healthy people.[6] Variation of TG and CE in urine samples is also expected to be a diagnostic marker for bladder cancer.[7]

Among various body fluid samples for lipidomic research, the serum is the first choice because it contains rich lipid molecules and is widely used in clinical trials.[8] The major platform for serum lipidomic research is liquid chromatography−mass spectrometry (LC−MS),[9] which is able to detect high coverage of lipid molecules owing to the good separation ability of LC. Especially, the development of 2D-LC has further improved its sensitivity and accuracy to detect low-abundance lipids. For example, 2D-LC can already detect more than 700 lipids in human plasma.[10] Untargeted lipid analysis of human plasma across nine LC−MS platforms in the positive ion mode showed that 307 lipids in human plasma could be annotated.[11] However, lipid analysis on LC−MS platforms is usually time-consuming, constituting a major limitation in large-scale clinical practice and disease screening. Surface-assisted laser desorption ionization mass spectrometry (SALDI-MS) is a high-throughput platform, which can analyze each sample within a few seconds.[12] In SALDI-MS analysis, laser desorption and ionization (LDI) of small molecules could take place on the surface of nanomaterials without the need for

Received: November 12, 2021
Accepted: May 25, 2022

traditional organic matrices, eliminating the high background and "sweet spot" effect caused by inhomogeneous crystallization. Recently, a novel organic matrix with low background and a uniform matrix coating has been reported, but this work only focused on the negative ion mode.[13] Therefore, nanomaterials with low background, high sensitivity, high coverage, and high reproducibility still need to develop in SALDI-MS.[14−17] Our previous work demonstrated that vertical silicon nanowires (VSiNWs) displayed unique advantages owing to their large surface area, high laser absorption efficiency, charge transferability, and appropriate thermal conductivity.[18,19] Based on this platform, nontargeted profiling of lipids and metabolites in tissues, cells, and saliva for disease diagnosis and cell subtype discrimination has been successfully achieved.[19−21] However, the primary problem encountered with the SALDI-MS platform is the low coverage of lipid signals due to the selectivity of nanomaterials to specific classes of lipid species in the positive ion mode. For example, the LDI process on VSiNWs is more selective to positively charged polar lipids, which significantly inhibits the signal of neutral lipids.[19,20] In contrast, metal nanoparticles, graphene oxide, and nanopost arrays (NAPAs) are more selective to neutral lipids but may inhibit the signal of polar lipids.[14,16,22] To solve the above problems, a combination of multiple matrices has been developed to expand the lipid coverage in SALDI-MS detection. For example, NAPA and DHB have been employed to selectively increase the TG and PC signals in the positive ion mode, respectively, resulting in high coverage in tissue mass spectrometry imaging.[22] However, the detection time also significantly increased when different types of matrices were sequentially used. Recently, CHCA and potassium salt precoated NAPAs were developed for mapping tissue phospholipids and neutral lipids in the positive ion mode.[23] However, it is difficult to analyze lipids below 700 Da owing to the high background of CHCA. In the case of serum lipid profiling, the coverage of lipid further reduces because the concentration of several types of lipids is lower in serum than that in tissues. So far, only 41 serum lipids covering five categories were detected on the SALDI-MS platform when only one type of nanomaterial was employed.[24] The number is far less than that obtained on the LC−MS platform, which can easily detect an average of 300 lipid metabolites in the positive ion mode.[11] Therefore, the development of new SALDI materials for high-coverage detection of serum lipids is urgently needed for large-scale serum lipidomic screening.

In the present work, a hybrid SALDI material was developed to achieve high-coverage detection of serum lipids. By modifying AuNPs on VSiNWs, charge-driven desorption accompanied by thermal-driven desorption could be achieved. Under the excitation of ultraviolet light, the surface hot-electrons of AuNPs can be transferred to the P-type semiconductor VSiNW,[25] resulting in Coulomb repulsion between the hole-rich AuNPs and positively charged analytes. This repulsion force causes the charge-driven desorption process to charged analytes without inhibiting the thermal desorption of neutral analytes. However, AuNPs themselves could produce strong background signals under laser irradiation due to the formation of charged Au nanocluster. To tackle this problem, a polydopamine film was coated on the surface of the hybrid nanomaterial to suppress background peaks.[26] At the same time, the PDA film also enhances the laser desorption process owing to its good UV absorption ability.[24] With this composite nanomaterial, low background, high coverage, and high reproducibility were achieved on the novel SALDI-MS platform for detection of serum lipids. The lipid peak number (S/N ≥ 5) detected in the positive ion mode reached 236, among them, and 107 lipid peak signals were identified. When combined with the negative ion mode, a maximal of 479 lipid peaks in serum samples could be acquired. To demonstrate its potential applicability in clinical diagnosis, serum samples from 57 hepatocellular carcinoma (HCC) patients and 76 healthy controls were collected and their serum lipids were profiled. With the assistance of statistical algorithms, HCC patients and healthy controls could be successfully discriminated based on a panel containing 14 features, which cover 8 classes of lipids. Investigation of the lipidomic-based diagnostic model in large-scale clinical cohorts will be conducted in our future work.

EXPERIMENTAL SECTION

Reagents and Materials. The following analytical reagents including tetrabutylammonium iodide (TBAI, ≥98%, CAS: 311-28-4) and TAG (17:0/17:0/17:0) were purchased from Sigma-Aldrich (Shanghai, China); PC (17:0/17:0), PC (18:0/18:0), and TAG (16:0/16:0/16:0) were purchased from Aladdin (Shanghai, China). More reagents for material preparation and serum extraction are shown in the Supporting Information.

Preparation of AuNPs. The preparation process of AuNPs adopted the traditional sodium citrate reduction method.[27] Briefly, 50 mL of 0.01% $HAuCl_4$ solution was heated to boiling with vigorous stirring. Then, 415 μL of 1% sodium citrate solution was rapidly added and boiling was continued for 30 min. Finally, a wine-red colloidal solution was formed.

Preparation of the VSiNW-Au-PDA Target for SALDI-MS. VSiNW-Au-PDA was prepared by a stepwise self-assembly method. First, VSiNWs were prepared by a one-step MACE method. In brief, p-type single-crystal silicon (5−10 Ω·cm) was cut into a square with a size of 2 cm × 2 cm by a diamond knife and then etched for 10 min in a solution containing 4.8 M HF and 0.02 M $AgNO_3$. (Caution: HF is highly toxic and volatile, which is harmful to the respiratory system and skeleton. Contacting HF with skin should be avoided, and all of the etching experiments need to be performed carefully in a fume hood.) After etching, the chip was washed three times with deionized water and then immersed in diluted HNO_3 (HNO_3/H_2O = 1:1) for 1 h to dissolve the Ag catalyst. After that, the as-prepared VSiNW wafer was treated with oxygen plasma and then reacted with a toluene solution containing 2% APTES at room temperature for 15 min. At the end of the reaction, the chip was washed with toluene and ethanol successively and stabilized at 100 °C for 1 h. The prepared VSiNW-APTES was immersed in the AuNP colloidal solution, kept for 150 min, then washed with deionized water, and dried under a N_2 stream. Finally, VSiNW-Au was then dipped into a dopamine solution (0.1 M in 50 mM Tris buffer, pH = 8.5) for 15 min. The coated material was taken out, rinsed with deionized water, and then blew-dried again with the N_2 stream.

Characterization of Materials. The sample morphology was characterized by a Hitachi's new-generation SU8010 field emission scanning electron microscope (FESEM, Hitachi SU8010, Japan) at an accelerating voltage of 3 kV. Elemental distribution on the surface of the material was characterized by energy-dispersive X-ray spectroscopy (EDS). X-ray photoelectron spectroscopy (XPS) measurements were performed

https://doi.org/10.1021/acs.analchem.1c04929
Anal. Chem. XXXX, XXX, XXX−XXX

Scheme 1. Schematic Illustration of the Preparation of VSiNW-Au-PDA

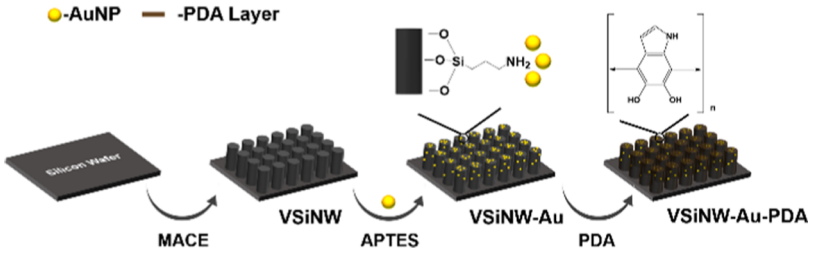

on an ESCALAB MKII X-electron spectrometer (VG Scientific) using a monochromatic Mg Kα X-ray source ($h\nu$ = 1253.6 eV). The surface chemistry of the material was analyzed by Fourier transform diffuse reflectance infrared spectroscopy (Nicolet iS10, Thermo Scientific). The morphology of AuNPs was characterized by transmission electron microscopy (TEM, H-7650, Hitachi Co.) at an accelerating voltage of 80 kV. A UV−vis spectrophotometer (Shanghai Spectrum, China) was used to record the UV absorption of AuNPs and Au-PDA in the range of 350−700 nm. The size of AuNPs was measured using a dynamic light scattering (DLS) instrument (ZEN3600, Zetasizer Nano ZS, Malvern, U.K.). Transient photovoltage (TPV) measurements were performed on a CEL-TPV2000 instrument (China).

Preparation of the Standard Sample for Evaluation of Mass Spectrometric Efficiency. Benzylpyridine hydrochloride (BP) and TBAI were used for studying the desorption mechanism on SALDI targets. BP was synthesized by the reaction of pyridine and benzyl chloride.[28] The detailed information is given in the Supporting Information. TBAI (5×10^{-8} M) were dissolved in a 40% MeOH/H_2O solution. To evaluate the sensitivity and selectivity for lipid detection on different SALDI-MS targets, a solution of mixed lipid standard samples including PC (17:0/17:0), PC (18:0/18:0), TAG (16:0/16:0/16:0), and TAG (17:0/17:0/17:0) was dissolved in $CHCl_3$, in which the concentration of each component was 0.1 mg/mL.

Serum Sample Collection. The quality control sample serum was prepared by combining the serum samples of 50 healthy people. These human serum samples were provided by the Second Affiliated Hospital of Zhejiang University School of Medicine. Patient serum with HCC and healthy controls were collected from Sir Run Run Shaw Hospital of Zhejiang University School of Medicine. Ethics approval was obtained from the ethics committee of Sir Run Run Shaw Hospital (No. 20200210-217).

Serum Lipid Extraction. Lipid extraction from serum samples was performed according to a modified Matyash method.[29] In brief, 40 μL of serum sample was added to 335 μL of MTBE/MeOH solution, vortexed for 10 min, and then 65 μL of H_2O was added. After vortexing the mixture for 10 min, it was centrifuged for another 10 min. Finally, the supernatant was collected and dried under a nitrogen stream. Before analysis, the pellet was reconstituted in 40 μL of isopropanol and stored at −20 °C.

Methods for SALDI-MS Detection. VSiNW and VSiNW-Au-PDA chips were further cut into small chips of a size of 3 mm × 3 mm. Two mocroliters of standard solution or serum lipid extraction was pipetted onto the chips, which were fixed with carbon conductive glue on an aluminum plate matched with the target chamber of a Bruker MALDI-TOF-MS. The SALDI-MS detection of probe molecules and standard samples on pure AuNPs was performed by mixing 2 μL of AuNP solution and 2 μL of samples, then dropping the mixture onto a steel target plate, and drying before MS detection. The SALDI mass spectrum was obtained on an UltrafleXtreme MALDI-TOF-MS instrument (Bruker, Germany) equipped with a 355 nm Nd:YAG laser beam. The laser parameters are set as follows: pulse width, 3 ns; peak power, <170 W; repetition rate, 1000 Hz. The pulse energy of the circular laser spot with a diameter of 100 μm was 3 μJ. Relative laser energy is defined as a percentage of pulse energy. The measurement mode was set to reflection mode. Other instrument parameters are set as follows: 100 ns of delayed extraction time and 19 kV (ion source 1) and 16.75 kV (ion source 2) of acceleration voltage. Each spectrum was obtained by an accumulation of 500 laser shots on a single point, and four spectra acquired on different points were superimposed to obtain the final mass spectrum. The calibrator for small-molecule mass spectrometry sampling was CHCA solution, and the calibrator for serum lipid samples was lipid standard mixed solution. The mass range was set at m/z = 400−1000 for negative ion and positive ion detection modes. The identification of serum lipids was achieved through the combination of MALDI-TOF/TOF, LC−MS/MS (AB Triple-TOF 5600plus System), and the LIPID MAPS database (http://www.lipidmaps.org). The detailed information is given in the Supporting Information.

Statistical Analysis. The data set consisted of average data of each sample through three repeated measurements. First, FlexAnalysis 3.4 software (Bruker Daltonics Corp.) was used to perform baseline subtraction pretreatment on the original mass spectrum. Then, the intensity of the selected peaks with S/N ≥ 5 was normalized to the total ionic intensity. Combining the two-sample Student's t-test in MATLAB software and the results of orthogonal partial least squares discriminant analysis (OPLS-DA) in SIMCA software (Umetrics AB, Umea, Sweden), the important peak information that satisfies both $P < 0.05$ and VIP > 1 was screened out. Then, the random forest packet in R software (randomForest; http://cran.r-project.org/web/packages/randomForest/) was used to further screen the above peak information, and the peak information with high contribution was screened out (Figure S1). Finally, the diagnostic model was constructed based on the selected data set. An artificial neural network (ANN) model with a multilayer perception structure (the number of hidden neurons is 10) was established in the pattern recognition tool of MATLAB software. In the ANN model, the training set occupied 70% of the total data set, and 15% of the data was used as the validation set. Another 15% of the data was used as the test set to evaluate the sensitivity and specificity of prediction.

https://doi.org/10.1021/acs.analchem.1c04929
Anal. Chem. XXXX, XXX, XXX−XXX

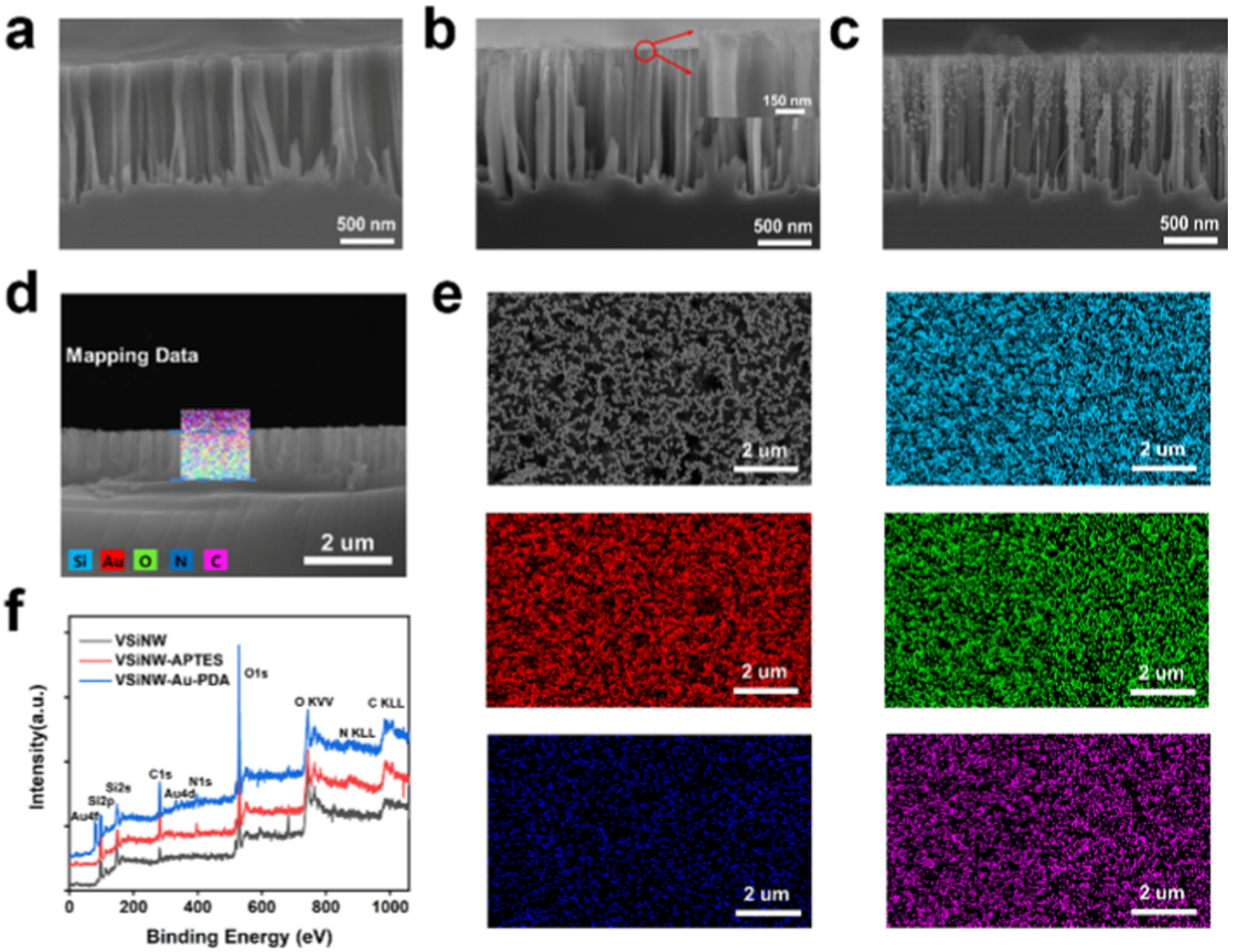

Figure 1. Characterization of materials. (a) Cross-sectional SEM images of VSiNW, (b) VSiNW-Au, and (c) VSiNW-Au-PDA (the scale bar is 500 nm); (d) cross-sectional and (e) top-view EDS elemental mapping images of VSiNW-Au-PDA; and (f) XPS spectrum of VSiNW-Au-PDA.

RESULTS AND DISCUSSION

Preparation and Characterization of VSiNW-Au-PDA.

AuNPs were prepared by the traditional sodium citrate reduction method.[27] TEM (Figure S2), DLS, and UV−vis analyses (Figure S3) showed that the average diameter of AuNPs was about 21 nm with uniform particle size. The slight red shift for the extinction peak of Au-PDA was due to the increase of refractive index around AuNPs after PDA coating (Figure S4). VSiNWs were prepared by a one-step metal-assisted chemical etching (MACE) method. The procedure for preparation of VSiNW-Au-PDA composites is illustrated in Scheme 1.

The morphologies of VSiNW (Figure 1a), VSiNW-Au (Figure 1b), and VSiNW-Au-PDA (Figure 1c) were characterized by SEM. The VSiNWs display a vertical nanopillar array structure with an average length of 1.1 μm and an average diameter of 70 nm (Figure 1a). The cross-sectional view of VSiNW-Au showed that the adhesion of AuNPs was thin and uniformly distributed without obvious agglomeration (Figure 1b). After immersion in a dopamine solution, the size of particles attached to the wall of VSiNW increased significantly, indicating the successful coating of PDA films on AuNPs (Figure 1c). EDS elemental analyses (Figure S5) and mapping images (Figure 1d,e) confirmed the existence of Si, Au, C, O, and N elements on the top side of VSiNW-Au-PDA. As both N and O elements were from APTES and PDA, XPS analysis was also performed to confirm the successful modification of APTES and PDA films on VSiNWs. A clear N 1s peak signal was shown in VSiNW-APTES and VSiNW-Au-PDA samples compared to that in freshly etched VSiNW (Figure 1f). In addition, the high-resolution spectra of N 1s (Figure S6a and Table S1) also showed the existence of free amine ($-NH_2$) groups and hydrogen bonds of $-NH_2$ groups, which proved the successful modification of APTES. The obvious Au 4f and Au 4d characteristic peaks in VSiNW-Au-PDA indicated that AuNPs were successfully modified on VSiNW (Figure 1f). The high-resolution spectra of C 1s and N 1s of VSiNW-Au-PDA (Figure S6b and Table S1) showed that functional groups such as C−C, C−N, C═O, ═NR, and R−NH−R were introduced on the surface, indicating the presence of catechol and quinone groups derived from PDA films. Furthermore, the presence of PDA on VSiNW-Au-PDA was also confirmed by diffuse reflectance infrared spectroscopy (DRIFTS). The observed broadband peaks at 3700−3300 cm^{-1} were assigned to ν(N−H) and ν(O−H) stretching modes, while 2924 and 2852 cm^{-1} were assigned to aliphatic ν(C−H) stretching. Absorption peaks at 1614 and 1468 cm^{-1} and at 1572 cm^{-1} were assigned to ν_{ring}(C═C) and ν_{ring}(C═N) stretching, respectively

https://doi.org/10.1021/acs.analchem.1c04929
Anal. Chem. XXXX, XXX, XXX−XXX

(Figure S7). The positions of these peaks were consistent with those observed in the reference spectra of dopamine.[30] The above results substantially confirmed the successful preparation of VSiNW-Au-PDA composites.

Performance of VSiNW-Au-PDA as the SALDI-MS Target. Before the SALDI-MS detection, the background peaks originating from VSiNW-Au-PDA were recorded. In the positive ion mode, VSiNWs show almost no background peaks within the molecular weight between 400 and 1000 Da. After modification with AuNPs (VSiNW-Au), several noisy peaks were observed in the positive ion mode. Among them, the peak at m/z = 590 belongs to the Au cluster ions of Au_3^+ (Figure 2a). In contrast, these background peaks disappeared when the VSiNW-Au-PDA target was used, indicating the significant role of PDA in suppressing the background of Au cluster ions.

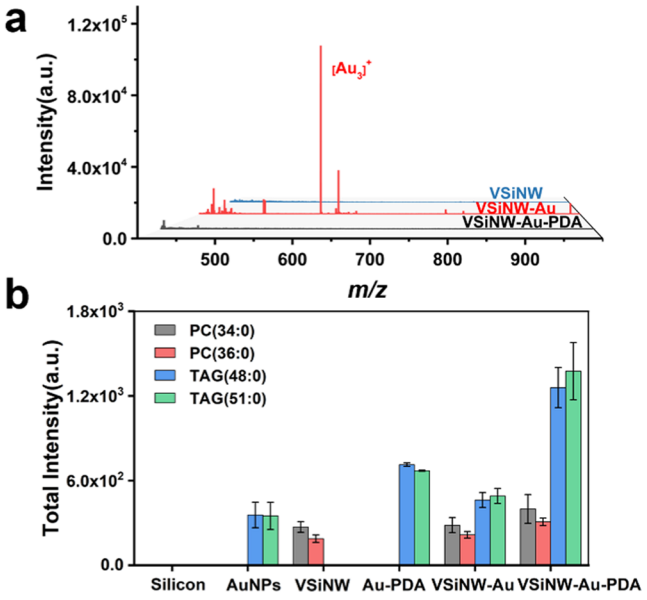

Figure 2. Background signal and SALDI-MS performance on different materials. (a) Background spectra of VSiNW, VSiNW-Au, and VSiNW-Au-PDA for LDI-MS analysis. The relative laser energy during detection is 60%. (b) Intensity of PC (34:0), PC (36:0), TAG (48:0), and TAG (51:0) in the lipid standard mixture solution on different materials. The relative laser energy during detection is 60%.

To compare the LDI performance of different types of materials in the detection of multiple lipids, a standard lipid mixture containing two TAG molecules and two PC molecules was prepared and subjected to SALDI-MS analysis. Silicon could not detect PC and TAG molecules due to its low desorption/ionization efficiency. When mere AuNPs were employed, only TAG signals could be detected, while the signal of positive charge lipids was inhibited (Figures 2b and S8). The results are in accordance with the finding of previous works, which indicated that AuNPs could promote the LDI efficiency of neutral lipids.[16] The phenomena might be ascribed to negatively charged hot electrons on the surface of AuNPs under laser irradiation.[31] On the contrary, VSiNW can sensitively detect PC but the TAG signal was suppressed. The detailed mechanism will be discussed in a later section. Au-PDA can only produce higher TAG signals than AuNPs, rather than expanding the coverage of detected lipids. In contrast, VSiNW-Au can simultaneously detect TAG and PC molecules, showing the combined merit of both materials. VSiNW-Au-PDA also displayed the same advantage as VSiNW-Au. Furthermore, the intensity of the TAG signal on VSiNW-Au-PDA was remarkably improved compared to that on VSiNW-Au probably owing to the enhanced UV absorption and photothermal transition efficiency of the PDA-coated surface.

Mechanistic Study. To further study the desorption mechanism on different types of materials, a chemical thermometer benzylpyridinium ion (BP^+) was used to probe the relative temperatures on the SALDI surfaces. It is well known that with an elevated temperature, BP^+ will undergo simple bond dissociation, leading to the formation of a benzyl cation (m/z 91.1) and a neutral pyridine fragment (Figure 3a).[32] The total ion intensity (TII) calculated by $I_{m/z\ 170.1}$+ $I_{m/z\ 91.1}$ can be used to express the desorption efficiency; the survival yield (SY) calculated by $I_{m/z\ 170.1}/(I_{m/z\ 170.1} + I_{m/z\ 91.1})$ can be related to the temperature of the SALDI target.[32] The graph of TII and SY of BP^+ on different types of materials under different relative laser energies is shown in Figure 3b. We can find that VSiNW has a higher desorption efficiency than AuNPs. Compared with that of bare AuNPs, the desorption efficiency of VSiNW-Au significantly improved. It should be noticed that the desorption efficiency of VSiNW-Au-PDA further increased due to the ability of PDA to absorb ultraviolet light.[24] According to the well-known thermal-driven desorption mechanism, with an increase of relative laser energy, the TII of BP^+ will accordingly increase because of high temperature, whereas the SY will decrease with an increase of relative laser energy, owing to the breakdown of chemical bonds.[31,33] In the present work, VSiNW has the highest desorption efficiency and the lowest SY. Therefore, the desorption behavior of BP^+ on VSiNW is exactly in accordance with the thermal-driven desorption mechanism. Interestingly, both TII and SY of BP^+ generated on VSiNW-Au and VSiNW-Au-PDA were significantly higher than those of AuNPs, when the relative laser energy was less than or equal to 60%. This phenomenon contradicts the thermal-driven desorption mechanism but is consistent with the charge-driven desorption mechanism proposed by Cheng et al.[31] To verify that the composite of VSiNW and AuNPs does involve the charge-driven desorption mechanism, tetrabutylammonium cation (TBA^+) was selected as a highly sensitive probe to the holes.[34] Compared with VSiNW and AuNPs, higher TBA^+ intensity was observed on VSiNW-Au composites (Figure 3d), confirming the involvement of the charge-driven desorption mechanism. On the composite of VSiNW-Au-PDA, the intensity of TBA^+ doubled, indicating that PDA film with high UV absorption capability could further promote the charge-driven desorption process. If the relative laser energy is more than 60%, VSiNW-Au-PDA has high TII and low SY (Figure 3b,c), showing a typical thermal-driven desorption mechanism. The results could be ascribed to the sharp increase of material temperature under higher laser energy. Under this condition, thermal-driven desorption dominates the overall ion desorption, thus weakening the contribution of charge-driven desorption. Therefore, to better achieve the simultaneous detection of positively charged analytes and neutral analytes, the relative laser energy should be less than 60%.

When AuNPs are excited by a laser, both hot electrons and holes are generated within 1−100 fs, and energy spreads rapidly on their surface. However, since the lifetime of holes is shorter than that of hot electrons,[31] a certain negative charge can be accumulated on their surface, resulting in the

https://doi.org/10.1021/acs.analchem.1c04929
Anal. Chem. XXXX, XXX, XXX−XXX

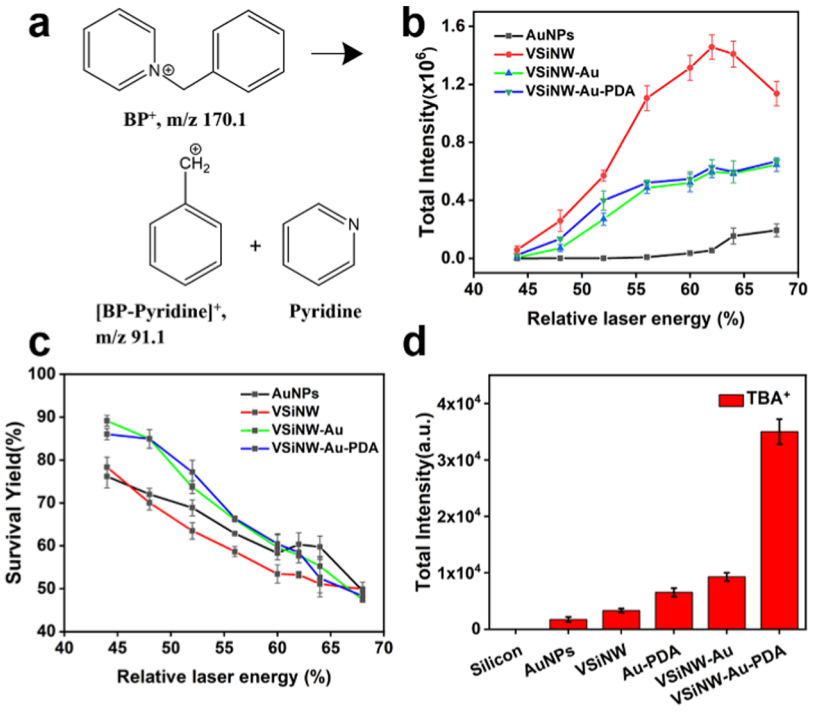

Figure 3. MS data for proving the dual-mechanism-driven SALDI-MS. (a) Bond cleavage of BP^+ resulting in the formation of $[BP\text{-pyridine}]^+$ and pyridine. Total ion intensity (b) and survival yield (c) of BP^+ detected on AuNPs, VSiNW, VSiNW-Au, and VSiNW-Au-PDA under different relative laser energies. (d) Intensity of TBA^+ on different materials and the relative laser energy during detection of 50%.

suppressed desorption of the positively charged analyte due to the electrostatic interaction. In this case, for the neutral molecules, thermal-driven desorption may overwhelm charge-driven desorption, leading to the enhanced signal of neutral molecules.[16] When VSiNW is excited by a laser, the increasing acidity of Si−OH groups on the surface facilitates the transfer of hydrogen ions to nitrogen-containing molecules and promotes their ionization efficiency.[35] In the meantime, thermal-driven desorption of positively charged ions will consume most of the thermal energy and suppress the desorption of neutral analytes. For the composite of VSiNW-AuNPs, the hot-electrons caused by AuNPs are easy to jump into the conduction band of p-type VSiNW under laser irradiation (Figure 4) and then undergo recombination with holes in p-type VSiNW.[25,36,37] This charge transfer process was verified by transient photovoltage (TPV) (Figure S9). The TPV response for VSiNW is negative, indicating photoinduced electron accumulation on the surface of VSiNW. The phenomenon is consistent with the results reported in other literature works.[38] Our previous work also proved that electrons could accumulate on the SiNWs upon laser irradiation, leading to electron transfer from SiNWs to the analyte.[18] As for VSiNW-Au and VSiNW-Au-PDA, the TPV response showed a negative value in the first stage and then changed to a positive value in a later stage because the hot electrons can be rapidly generated on the surface of AuNPs upon laser irradiation and then gradually transfer to VSiNW, leading to the accumulation of positively charged holes on the AuNP surface. The accumulation of holes results in a positively charged metal surface. The Coulombic repulsion between the AuNP surface and the positively charged analyte improves the contribution of the charge-driven process, thereby enhancing the peak intensity of the positively charged analyte. Under this circumstance, the thermal energy can still allocate to neutral analytes without weakening their peak signals.

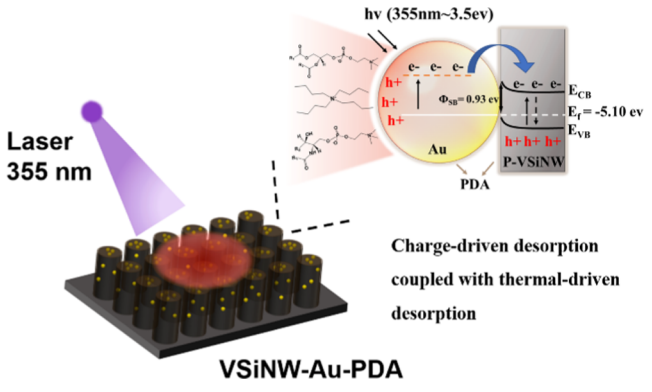

Figure 4. Dual-mechanism-driven desorption mechanism of VSiNW-Au-PDA under laser excitation. The positive charge on the AuNP surface plays a major role in charge-driven desorption, whereas the heat generated on VSiNW mainly contributes to thermal-driven desorption.

VSiNW-Au-PDA as the SALDI-MS Target for Serum Lipidomic Analysis. To further investigate the coverage of lipid detection on the SALDI-MS platform, a quality control (QC) sample originating from mixed serum samples collected from 50 healthy people was employed to evaluate the performance of different SALDI targets. When AuNPs were used, the major lipid species detected in the QC sample was TAG with a total peak number of 82 in the positive ion mode (Figures 5a and S10). The behavior is quite similar to that obtained from the standard sample and other literature works.[16] In addition, excessively background signals originating from the Au cluster ion peak lead to the significant interference with MS signals of lipid molecules. On contrary, high PC signal

https://doi.org/10.1021/acs.analchem.1c04929
Anal. Chem. XXXX, XXX, XXX−XXX

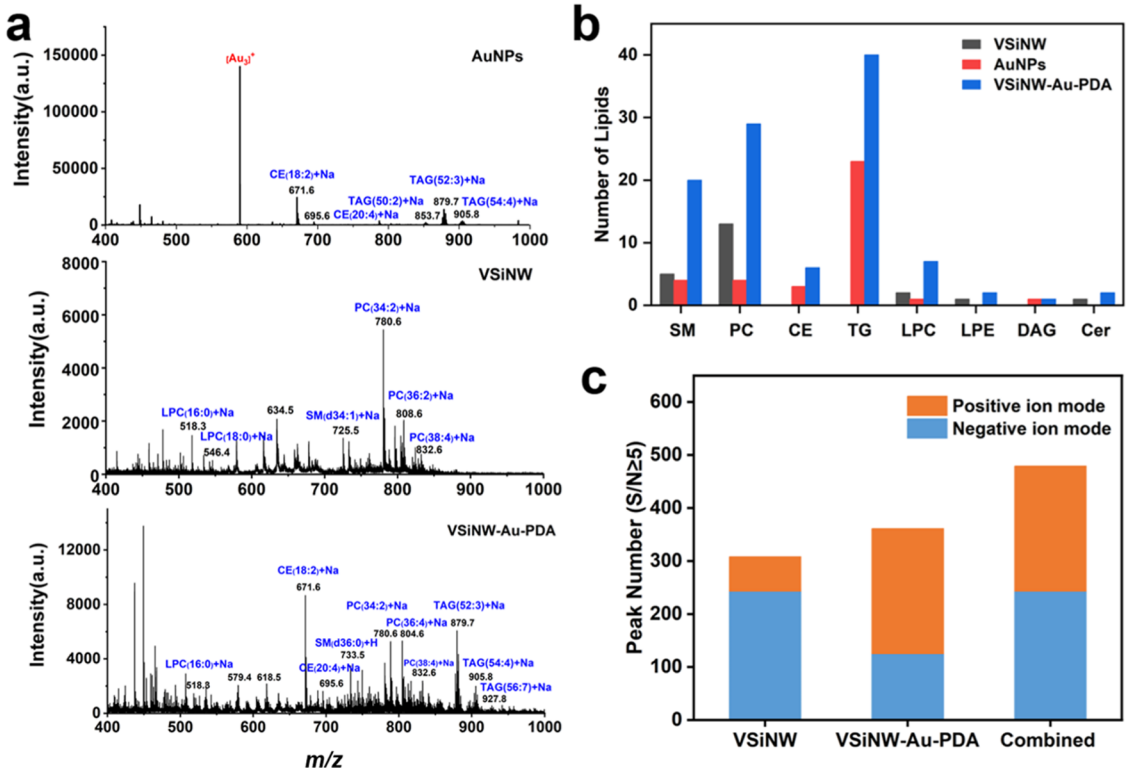

Figure 5. VSiNW-Au-PDA as the SALDI-MS target for serum lipidomic analysis. (a) LDI mass spectra of human serum lipid extract obtained on Au, VSiNW, and VSiNW-Au-PDA in the positive ion mode when using a relative laser energy of 60%. (b) Difference in the number of serum lipids detected by three materials: Au, VSiNW, and VSiNW-Au-PDA. (c) Total peak numbers (S/N ≥ 5) of VSiNW and VSiNW-Au-PDA and their combination in serum lipid LDI-MS analysis.

can be obtained on VSiNW, whereas the signal of neutral lipid was absent. The total peak number produced on the VSiNW chip was around 65. When VSiNW-Au-PDA was used, the number of effective peaks (S/N ≥ 5) reached ∼236, which included both neutral lipids (TAG, CE) and polar lipids (PC, SM) peaks. Compared with AuNPs and VSiNW, the number of effective peaks and types of lipid species detected on VSiNW-Au-PDA significantly increased, proving the synergistic effect of the composite material (Figures 5b and S10). In addition, the sensitivity and coverage for lipid detection on VSiNW-Au-PDA are even better than those on DHB, a traditional MALDI matrix for lipid detection (Figure S11). To further investigate the repeatability of serum lipid profiling, intrabatch and interbatch experiments were performed on VSiNW-Au-PDA and DHB, respectively. When DHB was used as the matrix, the median intra- and interbatch RSDs are 17.2 and 32.8%, respectively. In contrast, the median intra- and interbatch RSDs obtained on VSiNW-Au-PDA are 11.9 and 17.8%, respectively (Figure S12). The results indicate that the crystalized DHB may have irregular "sweet spots" upon laser irradiation, causing the lower repeatability of MS detection.

Serum lipid peaks obtained on VSiNW-Au-PDA were identified by MALDI-TOF/TOF, LC−MS/MS, and the LIPID MAPS database. Among 236 effective peaks, 107 lipid peaks were identified, and their molecule information is listed in Table S2. The SALDI-MS/MS spectra of some identified molecules are shown in Figures S13−S16. Around half of the lipid peaks are still not assigned, owing to the lower signal-to-noise ratio and the interference from isotope peaks. In contrast, compared with the results of previous research with only 41 serum detected lipids, the number of serum lipids significantly increased using the VSiNW-Au-PDA target. As far as we know, the number of 107 identified lipid peaks is the highest measured on the SALDI-MS platform in the positive ion mode. If measured in the negative ion mode, the signals of PI, PE, PG, and other lipids can be detected on the VSiNW-Au-PDA target, but it is inferior to VSiNW in terms of peak number (Figure S17). The reason for high MS intensity in the negative ion mode on the VSiNW has been investigated in our previous work.[18] To maximize the coverage of lipid detection, the VSiNW-Au-PDA target was used in the positive ion mode, whereas the VSiNW target was used in the negative ion mode. As a result, a total of 479 effective peaks (S/N ≥ 5) could be detected in human serum samples on the SALDI-MS platform (Figure 5c). Although the number of identified lipid species is still less than that obtained on the LC−MS platform,[11] these identified lipids detected on our platform have already covered eight classes of lipids, which include a medium and high abundance of glycerides, glycerophospholipids, sphingolipids, and cholesterol esters. These serum lipids play an essential role in the diagnosis of various diseases.[4,5] Moreover, high-speed serum lipid profiling can be achieved on the SALDI-MS platform. It costs only 40 min to detect a batch of 96 samples. If taking the time for sample pretreatment into consideration, the whole detection time is ∼90 min, which means that the time for each sample detection is less than 1 min. For the LC−MS platform, the detection time for each sample is at least 12 min.[39] In human lipidomics research, large sample numbers are often required to attain statistical results that could define associations between lipid species and disease phenotypes.[1] Therefore, the novel SALDI-MS platform will be superior in large-scale clinical lipidomic research.

https://doi.org/10.1021/acs.analchem.1c04929
Anal. Chem. XXXX, XXX, XXX−XXX

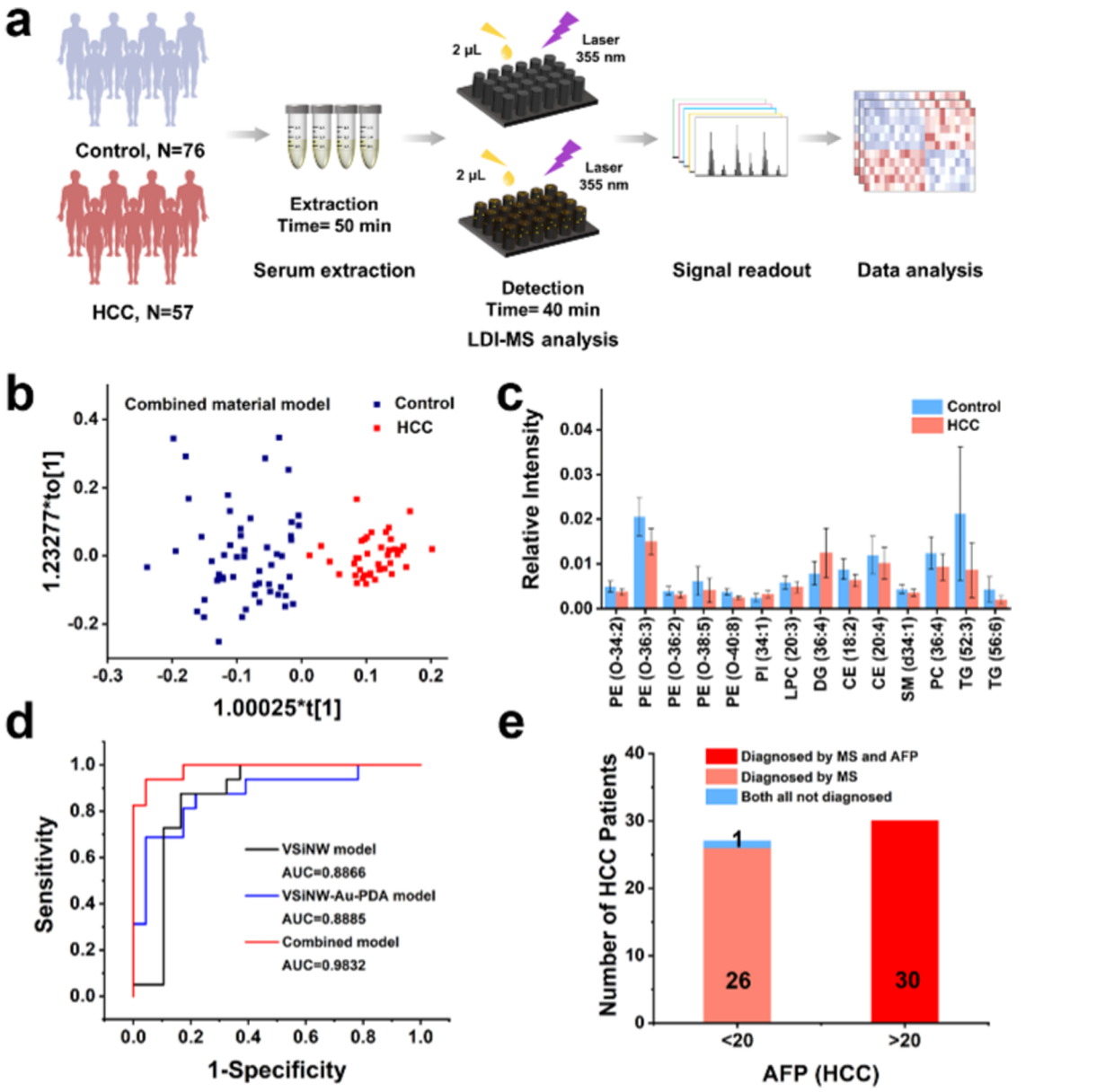

Figure 6. Analysis of serum lipids in patients with hepatocarcinoma (HCC) and healthy controls. (a) Schematic Illustration of serum lipidomic analysis of HCC patients and healthy controls by VSiNW and VSiNW-Au-PDA-assisted LDI-MS. (b) OPLS-DA results of serum samples from HCC patients and healthy controls in the training group based on the combined materials diagnostic model. (c) Change graph of the relative intensity of characteristic lipids in serum samples of HCC patients and healthy controls in the training group. (d) ROC curves of three models in the validation group. (e) Number of HCC patients diagnosed by AFP and MS models in all cohorts.

Analysis of Serum Lipids in Patients with Hepatocarcinoma (HCC) and Healthy Controls. HCC is the fourth most common cause of cancer-related deaths in the world,[40] and its morbidity and mortality are increasing rapidly. The liver plays a vital role in lipid metabolism because it regulates its synthesis and degradation. Once liver disease occurs, lipid metabolism will be disturbed. In recent years, considerable evidence has shown that there is a strong relationship between lipid metabolism and HCC.[40] Therefore, it is of great significance to explore serum lipid biomarkers for the early diagnosis of HCC. To evaluate the potential applications of the novel SALDI-MS target in clinical lipidomics, serum samples collected from 57 HCC patients and 76 healthy people were detected according to the workflow illustrated in Figure 6a. Among the 133 samples, 70% samples were assigned to the training group and 30% of samples were assigned to validation groups with a reasonable distribution of disease state, age, and gender (Table S3).

To evaluate the ability of lipidomic data to distinguish HCC patients from healthy controls, statistical methods including two-sample student's *t*-test, OPLS-DA, and random forest were combined, and 14 feature lipids were screened out for the classification model (Table S4). The feature lipids include five PE, two TG, one LPC, one DG, two CE, one SM, one PC, and one PI. OPLS-DA of the training group indicated good discrimination ability between the HCC and control groups (Figure 6b). The distribution of relative average intensity of these feature lipids in HCC patients and healthy controls is shown in Figure 6c.

https://doi.org/10.1021/acs.analchem.1c04929
Anal. Chem. XXXX, XXX, XXX−XXX

To demonstrate the superiority of high-coverage lipid data obtained on the combined materials, statistical analysis based on lipid data obtained on VSiNW and VSiNW-Au-PDA was also conducted, respectively. To ensure credible statistical comparisons, each statistical models were constructed from 14 feature lipids (Tables S5 and S6), which has the same feature number as the combined model. The results of OPLS-DA in both training groups show that the discrimination ability using one type of material alone displays weak predictive performance (Figure S18).

In addition, an artificial neural network was also used to evaluate the diagnostic accuracy of three models constructed on the data set from combined chips, VSiNW, and VSiNW-Au-PDA, respectively (Table S7). The results showed that the sensitivity and specificity of the model obtained on the combined chips in the validation group were 92.7 and 96%, respectively. In contrast, the sensitivity and specificity obtained on VSiNW were only 82.3 and 87.7%, while the sensitivity and specificity obtained on VSiNW-Au-PDA were only 75 and 91.3%, respectively, indicating the significance of high lipid coverage in the construction of an accurate diagnosis model. In addition, the ROC curves obtained on the combined chips achieved the highest AUC value among the three models in the validation group (Figure 6d). To better reflect the superiority of the lipidomic-based method in clinical diagnosis, the diagnostic accuracy obtained with this method was compared with that obtained with the AFP method in all cohorts. The results showed that our model could not only discriminate 30 AFP-positive (AFP > 20) HCC patients but also accurately diagnose 26 in 27 AFP-negative (AFP < 20) HCC patients (Figure 6e), indicating the significantly improved sensitivity for HCC diagnosis.[40] The perturbation pathways of lipids in the serum of HCC patients have been reported before.[39,40] For example, increased uptake of TG by liver cancer cells from serum may lead to decreased serum TG.[39] The decreased PE-*N*-methyltransferases (PEMT) activity in liver cancer patients will lead to a decrease in polyunsaturated PC and hemolysis.[41] Overexpression of lysophospholipase D/autotoxin (ATX) will lead to a decrease in LPC,[42] while a decrease in serum lecithin-cholesterol acyltransferase (LCAT) activity will lead to a decrease in CE levels. The up- or downregulation of these lipids in the serum of HCC patients is consistent with the results in the present work, further supporting that the panel of serum lipids discovered in our platform might act as good omics biomarkers for HCC diagnosis. In addition, some unreported lipids such as DG (36:4) and SM (d34:1) were found; the pathways of these lipid perturbations will be studied in future works.

CONCLUSIONS

In summary, this work reported a novel SALDI-MS target, VSiNW-Au-PDA, as the high-speed, low-background, high-reproducibility, and high-coverage serum lipid detection platform in the positive ion mode. A series of probes and standard molecules were employed in the evaluation of LDI performance and mechanistic study. The results proved that the LDI-MS process on VSiNW-Au-PDA involved an enhanced charge-driven desorption mechanism in the positive ion mode, thereby contributing to high coverage detection of serum lipids. Simultaneous detection of 236 serum lipids including neutral lipids (TAG, CE) and polar lipids (PC, SM) can be achieved in the positive ion mode. Among them, 107 lipid peaks can be successfully identified. Upon combining the data obtained from the positive ion mode on VSiNW-Au-PDA and the negative ion mode on VSiNW, a maximum of 479 effective peaks assigned to eight classes of lipid could be detected. Based on the high coverage lipid data, a panel including 14 feature lipids was screened out for HCC diagnosis. With the assistance of statistical algorithms, the diagnostic model constructed on these 14 feature lipids could accurately discriminate between HCC patients and healthy controls in 133 samples. The newly developed SALDI-MS platform for high coverage of lipid detection might open a new avenue in the early clinical diagnosis based on lipid metabolism disorders.

ASSOCIATED CONTENT

Supporting Information

The Supporting Information is available free of charge at https://pubs.acs.org/doi/10.1021/acs.analchem.1c04929.

Experimental procedures, material characterization, standard product analysis, DHB analysis, material stability results, MS/MS identification of lipids, representative mass spectra, statistical analysis results, list of lipids in human serum extracts, clinical characteristics of the study cohort, lipid information for the diagnostic model, and artificial neural network statistical analysis results (PDF)

AUTHOR INFORMATION

Corresponding Authors

Xiao Liang − *Department of General Surgery, Sir Run Run Shaw Hospital, School of Medicine, Zhejiang University, Hangzhou 310016, China*; Email: srrshlx@zju.edu.cn

Jianmin Wu − *Institute of Analytical Chemistry, Department of Chemistry, Zhejiang University, Hangzhou 310058, China*; orcid.org/0000-0002-0999-9194; Email: wjmst1@zju.edu.cn

Authors

Xuetong Qu − *Institute of Analytical Chemistry, Department of Chemistry, Zhejiang University, Hangzhou 310058, China*

Tao Wang − *Institute of Analytical Chemistry, Department of Chemistry, Zhejiang University, Hangzhou 310058, China*

Xingyue Liu − *Institute of Analytical Chemistry, Department of Chemistry, Zhejiang University, Hangzhou 310058, China*

Xinrong Jiang − *Institute of Analytical Chemistry, Department of Chemistry, Zhejiang University, Hangzhou 310058, China*

Complete contact information is available at: https://pubs.acs.org/10.1021/acs.analchem.1c04929

Notes

The authors declare no competing financial interest.

ACKNOWLEDGMENTS

The authors acknowledge the financial support from the National Natural Science Foundation of China (Nos. 21575127 and 21874118).

ABBREVIATIONS

TG	triacylglycerol
CE	cholesterol ester
PC	phosphatidylcholine
SM	sphingomyelin
LPE	lysophosphatidylethanolamine

https://doi.org/10.1021/acs.analchem.1c04929
Anal. Chem. XXXX, XXX, XXX−XXX

PE phosphatidylethanolamine
LPC lysophosphatidylcholine
DAG diacylglycerol
Cer ceramide
PI phosphatidylinositol

REFERENCES

(1) Han, X. *Nat. Rev. Endocrinol.* **2016**, *12*, 668−679.
(2) Wolrab, D.; Jirasko, R.; Chocholouskova, M.; Peterka, O.; Holcapek, M. *TrAC, Trends Anal. Chem.* **2019**, *120*, No. 115480.
(3) Fahy, E.; Subramaniam, S.; Brown, H. A.; Glass, C. K.; Merrill, A. H.; Murphy, R. C.; Raetz, C. R. H.; Russell, D. W.; Seyama, Y.; Shaw, W.; Shimizu, T.; Spener, F.; van Meer, G.; VanNieuwenhze, M. S.; White, S. H.; Witztum, J. L.; Dennis, E. A. *J. Lipid Res.* **2005**, *46*, 839−861.
(4) Bandu, R.; Mok, H. J.; Kim, K. P. *Mass Spectrom. Rev.* **2018**, *37*, 107−138.
(5) Lu, J.; Lam, S. M.; Wan, Q.; Shi, L.; Huo, Y.; Chen, L.; Tang, X.; Li, B.; Wu, X.; Peng, K.; Li, M.; Wang, S.; Xu, Y.; Xu, M.; Bi, Y.; Ning, G.; Shui, G.; Wang, W. *Diabetes Care.* **2019**, *42*, 2117−2126.
(6) Yu, Z. T.; Chen, H. K.; Ai, J. M.; Zhu, Y.; Li, Y.; Borgia, J. A.; Yang, J. S.; Zhang, J. C.; Jiang, B.; Gu, W.; Deng, Y. P. *Oncotarget* **2017**, *8*, 107899−107906.
(7) Cruciani, G.; Pellegrino, R. M.; Veroli, A. D.; Cataldi, S.; Marocco, D.; Costantini, E.; Sidoni, A.; Viola-Magni, M. J. T. C. R. *Transl Cancer Res.* **2017**, *6*, 1197−1206.
(8) Vvedenskaya, O.; Wang, Y.; Ackerman, J. M.; Knittelfelder, O.; Shevchenko, A. *TrAC, Trends Anal. Chem.* **2019**, *120*, No. 115277.
(9) Yang, K.; Han, X. *Trends Biochem. Sci.* **2016**, *41*, 954−969.
(10) Koelmel, J. P.; Kroeger, N. M.; Gill, E. L.; Ulmer, C. Z.; Bowden, J. A.; Patterson, R. E.; Yost, R. A.; Garrett, T. J. *J. Am. Soc. Mass. Spectrom.* **2017**, *28*, 908−917.
(11) Cajka, T.; Smilowitz, J. T.; Fiehn, O. *Anal. Chem.* **2017**, *89*, 12360−12368.
(12) Abdelhamid, H. N. *Microchim. Acta* **2018**, *185*, 200.
(13) Shi, Y.; Hu, H.; Hao, Q.; Wu, R.; Wang, L.; Qin, L.; Gu, W.; Liu, H.; Jiang, D.; Hong, L.; Zhou, Y.; Liu, X.; Feng, J.; Xue, K.; Wang, X. *Chem. Commun.* **2022**, *58*, 633−636.
(14) Liang, K.; Gao, H.; Gu, Y.; Yang, S.; Zhang, J.; Li, J.; Wang, Y.; Wang, Y.; Li, Y. *Anal. Chim. Acta* **2018**, *1035*, 108−118.
(15) Iakab, A. S.; Rafols, P.; Garcia-Altares, M.; Yanes, O.; Correig, X. *Adv. Funct. Mater.* **2019**, *29*, No. 1903609.
(16) Dufresne, M.; Masson, J. F.; Chaurand, P. *Anal. Chem.* **2016**, *88*, 6018−6025.
(17) Abdelmaksoud, H. H.; Guinan, T. M.; Voelcker, N. H. *ACS Appl. Mater. Interfaces* **2017**, *9*, 5092−5099.
(18) Chen, X.; Wang, T.; Lin, L.; Wo, F.; Liu, Y.; Liang, X.; Ye, H.; Wu, J. *ACS Appl. Mater. Interfaces* **2018**, *10*, 14389−14398.
(19) Chen, X.; Gao, J.; Wang, T.; Jiang, X.; Chen, J.; Liang, X.; Wu, J. *Anal. Chem.* **2019**, *91*, 10376−10380.
(20) Wang, T.; Chen, X.; Luan, C.; Wu, J. *Anal. Chim. Acta.* **2020**, *1107*, 92−100.
(21) Jiang, X.; Chen, X.; Wang, T.; Li, Y.; Pan, A.; Wu, J. *Talanta* **2021**, *225*, No. 122022.
(22) Fincher, J. A.; Korte, A. R.; Dyer, J. E.; Yadavilli, S.; Morris, N. J.; Jones, D. R.; Shanmugam, V. K.; Pirlo, R. K.; Vertes, A. *J. Mass Spectrom.* **2020**, *55*, No. e4443.
(23) Dufresne, M.; Fincher, J. A.; Patterson, N. H.; Schey, K. L.; Norris, J. L.; Caprioli, R. M.; Spraggins, J. M. *Anal. Chem.* **2021**, *93*, 12243−12249.
(24) Yang, J.; Zhang, W.; Zhang, H.; Zhong, M.; Cao, W.; Li, Z.; Huang, X.; Nie, Z.; Liu, J.; Li, P.; Ma, X.; Ouyang, Z. *ACS Appl. Mater. Interfaces* **2019**, *11*, 46140−46148.
(25) Li, X.; Chen, X.; Tan, J.; Liang, X.; Wu, J. *Analyst* **2017**, *142*, 586−590.
(26) Kang, K.; Jang, H.; Kim, Y. K. *Analyst* **2017**, *142*, 2372−2377.
(27) Frens, G. *Nat. Phys.* **1973**, *241*, 20−22.
(28) Lai, S. K. M.; Tang, H. W.; Lau, K. C.; Ng, K. M. *J. Phys. Chem. C* **2016**, *120*, 20368−20377.
(29) Matyash, V.; Liebisch, G.; Kurzchalia, T. V.; Shevchenko, A.; Schwudke, D. *J. Lipid Res.* **2008**, *49*, 1137−1146.
(30) Zangmeister, R. A.; Morris, T. A.; Tarlov, M. J. *Langmuir* **2013**, *29*, 8619−8628.
(31) Cheng, Y. H.; Ng, K. M. *Anal. Chem.* **2020**, *92*, 5645−5649.
(32) Picca, R. A.; Calvano, C. D.; Cioffi, N.; Palmisano, F. *Nanomaterials* **2017**, *7*, 75.
(33) Lai, S. K.-M.; Tang, H.-W.; Lau, K.-C.; Ng, K.-M. *J. Phys. Chem. C* **2016**, *120*, 20368−20377.
(34) Cheng, Y. H.; Ng, K. M. *Anal. Chem.* **2020**, *92*, 10262−10267.
(35) Alimpiev, S.; Grechnikov, A.; Sunner, J.; Karavanskii, V.; Simanovsky, Y.; Zhabin, S.; Nikiforov, S. *J. Chem. Phys.* **2008**, *128*, No. 014711.
(36) Lee, J. S.; Shevchenko, E. V.; Talapin, D. V. *J. Am. Chem. Soc.* **2008**, *130*, 9673−9675.
(37) Dillon, J. A.; Farnsworth, H. E. *J. Appl. Phys.* **1958**, *29*, 1195−1202.
(38) Duzhko, V.; Timoshenko, V. Y.; Koch, F.; Dittrich, T. *Phys. Rev. B* **2001**, *64*, No. 075204.
(39) King, A. M.; Trengove, R. D.; Mullin, L. G.; Rainville, P. D.; Isaac, G.; Plumb, R. S.; Gethings, L. A.; Wilson, I. D. *J. Chromatogr. A* **2020**, *1611*, No. 460597.
(40) Lu, Y.; Chen, J.; Huang, C.; Li, N.; Zou, L.; Chia, S. E.; Chen, S.; Yu, K.; Ling, Q.; Cheng, Q.; Zhu, M.; Zhang, W.; Chen, M.; Ong, C. N. *Oncotarget* **2018**, *9*, 5032−5043.
(41) Chen, S.; Yin, P.; Zhao, X.; Xing, W.; Hu, C.; Zhou, L.; Xu, G. *Electrophoresis* **2013**, *34*, 2848−2856.
(42) Wu, J.-M.; Xu, Y.; Skill, N. J.; Sheng, H.; Zhao, Z.; Yu, M.; Saxena, R.; Maluccio, M. A. *Mol. Cancer* **2010**, *9*, 71.

https://doi.org/10.1021/acs.analchem.1c04929
Anal. Chem. XXXX, XXX, XXX−XXX